CHEMISTRY OF MATERIALS

Open Access

pubs.acs.org/cm

Article

Tailored Pnictogen Precursor Chemistry Enables Metal-Hydride-Free Selective Synthesis of $InP_{1-x}Sb_x$ Quantum Dots

Kazuhiro Nemoto,* Cong Zhang, Daiki Kido, Daniel Limouchi, Masaki Takeguchi, Hong-Tao Sun, and Naoto Shirahata*

Cite This: *Chem. Mater.* 2026, 38, 3486−3495

Read Online

ACCESS | Metrics & More | Article Recommendations | Supporting Information

ABSTRACT: Controlling precursor reactivity through ligand design remains a central challenge in the colloidal synthesis of III−V quantum dots (QDs). In particular, InSb QDs have been difficult to access due to hazardous metal-hydride reductants and limited precursor availability. Here, we report a metal-reductant-free route employing tris(dimethylamino)phosphine [$P(NMe_2)_3$], whose function as a reductant or a P(−III) source is determined by the coordination environment of $SbCl_3$. When Sb−oleylamine ($OlNH_2$) complexes are used, $P(NMe_2)_3$ reduces both Sb and In precursors, producing phase-pure InSb QDs. In contrast, Sb−trioctylphosphine (TOP) complexes undergo partial Sb(+III) reduction via electrons released from TOP oxidation, while $P(NMe_2)_3$ simultaneously reduces In and generates P(−III) species, enabling controlled formation of alloyed $InP_{1-x}Sb_x$ QDs ($0.6 \leq x < 1$). ^{31}P NMR and EXAFS analyses reveal that the Sb−TOP complex exists in a dynamic chloride−phosphine equilibrium, which governs P(−III) availability and reaction selectivity. This mechanistic insight demonstrates that ligand coordination can be leveraged to modulate precursor reactivity, selectively direct reduction pathways, and achieve controlled alloying in colloidal III−V QDs. The resulting QDs exhibit sharp excitonic absorption and band-edge emission in the short-wavelength infrared (SWIR) region, bridging the previously inaccessible spectral gap between InP and InSb. Beyond InSb and $InP_{1-x}Sb_x$, these findings establish a general design principle: dynamic ligand environments can be exploited to tune reactivity, composition, and alloy formation in colloidal semiconductors. This work thus provides a safe, high-yielding, mechanistically rational strategy for Sb-based III−V QDs and lays the foundation for extending optoelectronic functionality through precise precursor engineering.

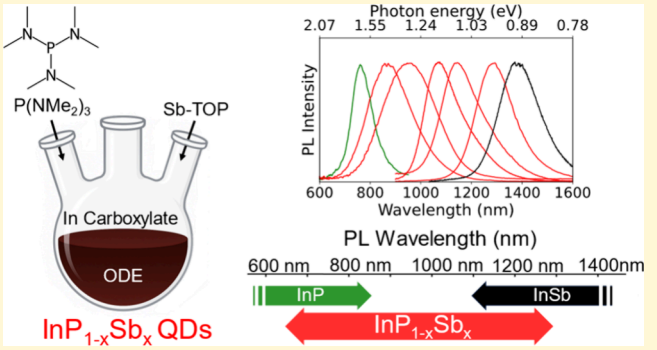

INTRODUCTION

Group III−V semiconductors are a class of RoHS-compliant materials distinguished by high carrier mobility, low electron effective mass and composition-tunable bandgaps achieved through alloying.[1] When processed as colloidal quantum dots (QDs), these materials exhibit strong quantum confinement effects, enabling a wide range of optoelectronic applications, including solar cells,[2,3] photodetectors,[4−6] light-emitting diodes,[7,8] and biomedical imaging.[9−11]

The colloidal synthesis of III−V QDs was pioneered in 1989 by Wells and co-workers,[12] who employed tris(trimethylsilyl)-arsenide as a pnictide precursor to generate InAs and GaAs QDs via dehalosilylation.[12,13] This highly reactive precursor chemistry was later extended to InP[14,15] and InSb QDs,[16,17] enabling fast nucleation and brief growth, narrow size distributions, and highly crystalline nanocrystals while generating volatile Si-containing byproducts that are readily removed after reaction.[8,18,19] Indeed, tris(trimethylsilyl)-phosphine (TMS−P) has long been the benchmark for InP QDs and enables near-unity photoluminescence quantum yield (PLQY) after shelling.[8] However, its rapid consumption during nucleation limits control over growth, hindering the formation of larger nanocrystals, and its pyrophoric, air sensitive nature poses significant safety concerns.[20] These limitations have stimulated efforts toward alternative precursor systems.

Aminophosphines have emerged as cost-effective and synthetically accessible pnictogen precursors suitable for QD synthesis.[21−23] In oleylamine, transamination generates tris-(oleylamino)phosphine in situ, which undergoes disproportionation to form both P(+V) and reactive P(−III) species.[21,22] The latter reacts with In(+III) to deliver InP units, enabling high-quality InP QDs with visible PLQYs exceeding 95% after

Received: December 4, 2025
Revised: March 24, 2026
Accepted: March 27, 2026
Published: April 2, 2026

shelling.[24−26] Extending this strategy to aminoarsines revealed limited reactivity: tris(oleylamino)arsine cannot undergo disproportionation to form As(−III) species.[27] This challenge was addressed by introducing aminophosphine, which reduces As(+V) to As(−III), as shown in equation[27]:

$$InCl_3 + As[NMe_2]_3 + 3P[NMe_2]_3 + 12RNH_2 \rightarrow InAs + 12HNMe_2 + 3[P(NHR)_4Cl] \quad (1)$$

In contrast, synthesizing colloidal InSb QDs remains particularly challenging due to lack of Sb(−III) such as stibine (SbH_3).[28] Reiss et al. reported that Sb(+III) can be reduced to Sb(−III) by In(+I),[29] but most successful syntheses rely on strong metal hydrides such as lithium triethylborohydride ($LiEt_3BH$)[30−39] These reagents coreduce Sb(+III) and In-(+III) to zerovalent species that nucleate InSb, as shown in equation:

$$In(0) + Sb(0) \rightarrow InSb \quad (2)$$

However, their high hydride donor ability ($\Delta G°_h$ = 26 kcal mol^{-1})[34] often leads to uncontrolled reduction and metallic byproducts, compromising control over nucleation and growth. Recent efforts have turned to milder hydrides,[35] such as Alane N,N-dimethylethylamine (AlH_3·DMEDA) with a weaker reducing ability of $\Delta G°_h$ = 37 kcal mol^{-1},[36,37] yet a metal-hydride-free synthesis of InSb QDs has not been demonstrated. Although $P(NMe_2)_3$ is much weaker reductant,[34] its ability to form InSb under QD synthesis conditions has remained unexplored.

Here, we report a metal-reductant-free route to phase-pure InSb QDs. As outlined in Scheme 1, $P(NMe_2)_3$ acts as a selective reductant that enables high-yield formation of InSb from indium palmitate [$In(Palm)_3$] and an $SbCl_n$−oleylamine complex (Sb−OlNH). Remarkably, replacing Sb−OlNH with an $SbCl_n$−trioctylphosphine complex (Sb−TOP) allows $P(NMe_2)_3$ to serve dually as both a reductant and a phosphorus source, yielding anion-alloyed $InP_{1-x}Sb_x$ QDs ($0.6 \leq x < 1$). The resulting QDs exhibit well-defined first excitonic absorption peaks and corresponding band-edge PL, demonstrating the effectiveness of this metal-reductant-free strategy.

Scheme 1. Schematic Illustration of the Precursor Chemistry and Reaction Concept Leading to the Selective Formation of $InP_{1-x}Sb_x$ QDs[a]

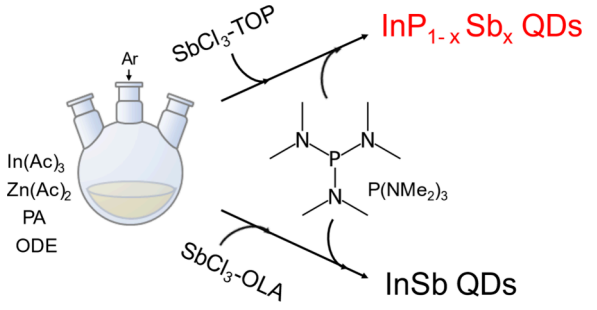

[a]Indium acetate ($In(Ac)_3$) is first converted into $In(Palm)_3$ through ligand exchange with palmitic acid in octadecene (ODE). The reaction mixture is then heated under an argon atmosphere, and the Sb precursor, the $P(NMe_2)_3$, and a small amount of $OlNH_2$ are added to generate either InSb or $InP_{1-x}Sb_x$ QDs. The final product can be selectively controlled by tuning the coordination environment of $SbCl_3$. When $SbCl_3$ is mixed with $OlNH_2$, InSb QDs are formed, whereas mixing $SbCl_3$ with TOP leads to the selective formation of $InP_{1-x}Sb_x$ QDs.

RESULTS

$InP_{1-x}Sb_x$ QDs ($0.6 \leq x \leq 1$) were synthesized using a modified hot-injection procedure adapted from established InP QD syntheses.[21,27,38] A schematic overview of the method is provided in Figure S1 (see Supporting Information). Building upon our preliminary findings (Section S1, Figure S2, Supporting Information), $In(Palm)_3$ served as the indium precursor and 1-octadecene (ODE) as the reaction solvent. We found that the coordination environment of the antimony precursor strongly affected the reducing ability of $P(NMe_2)_3$, leading to distinct final chemical composition of the QDs (Scheme 1). To identify suitable antimony precursors, we evaluated the solubility of several $SbCl_n$−L Lewis acid−base adducts in ODE—where L = trioctylphosphine (TOP), diphenylphosphine (DPP), or $OlNH_2$—and confirmed that both TOP and $OlNH_2$ form stable complexes with $SbCl_3$ (Section S2, Figures S3 and S4, Table S1, Supporting Information). Following the procedure outlined in Figure S1, $In(Palm)_3$ was heated with either Sb−OlNH or Sb−TOP at 190 °C in ODE under Ar atmosphere. A mixture of $P(NMe_2)_3$ and excess $OlNH_2$ (>3 equiv) was then swiftly injected to initiate nucleation. The resulting mixture was subsequently heated to 280 °C, maintained for 2 min, and cooled to room temperature. After the reaction, the crude solution was purified directly by centrifugation, yielding a supernatant (Mother sample) and an insoluble fraction (Precipitate). Precipitate consisted of macroscopic InSb crystals in both the OlNH- and TOP-based systems (Figure S5, Supporting Information). In contrast, Mother sample was separated into Samples A, B, and C via stepwise ethanol-induced fractionation (Section S3, Figures S6 and S7, Supporting Information).

Optimization of the synthetic conditions confirmed the formation of QDs in the mother sample (Section S4, Supporting Information). Specifically, the injection temperature of the Sb and P precursors was investigated. At temperatures below 140 °C, the balance between nucleation and growth could not be controlled, and almost no QDs were formed. In contrast, at temperatures above 240 °C, low-boiling $P(NMe_2)_3$ evaporated, leading to the preferential formation of readily reducible metallic Sb and a decrease in the yield of InSb QDs. Injection at 190 °C enabled the recovery of QDs without generating metallic impurities (Figure S8b, Supporting Information). Furthermore, as shown in Scheme 1, the simultaneous addition of a Zn source with $In(Palm)_3$ improved the size distribution (Figure S8b, Supporting Information).

XRD and TEM analyses were performed to elucidate the structural characteristics of Samples A−C prepared using the Sb−OlNH and Sb−TOP precursor systems. As shown in Figure 1a, Sample A from the Sb−OlNH route exhibits three diffraction peaks (green) corresponding to the (111), (220), and (311) planes of zinc-blende InSb. In contrast, Samples A from the Sb−TOP system show diffraction features positioned between those of InSb and InP, shifting systematically to lower 2θ values with increasing Sb/In feed ratio. This behavior is consistent with the formation of $InP_{0.4}Sb_{0.6}$ QDs (blue) and $InP_{0.2}Sb_{0.8}$ QDs (orange), matching theoretical predictions.[39,40] TEM analysis (Figures 1b and S9) revealed that the resulting $InP_{1-x}Sb_x$ QDs (x = 0.6−0.8) have mean diameters of 4.1 ± 1.6 and 4.2 ± 1.3 nm, respectively, indicating that variations in phosphorus content do not

https://doi.org/10.1021/acs.chemmater.5c03273
Chem. Mater. 2026, 38, 3486−3495

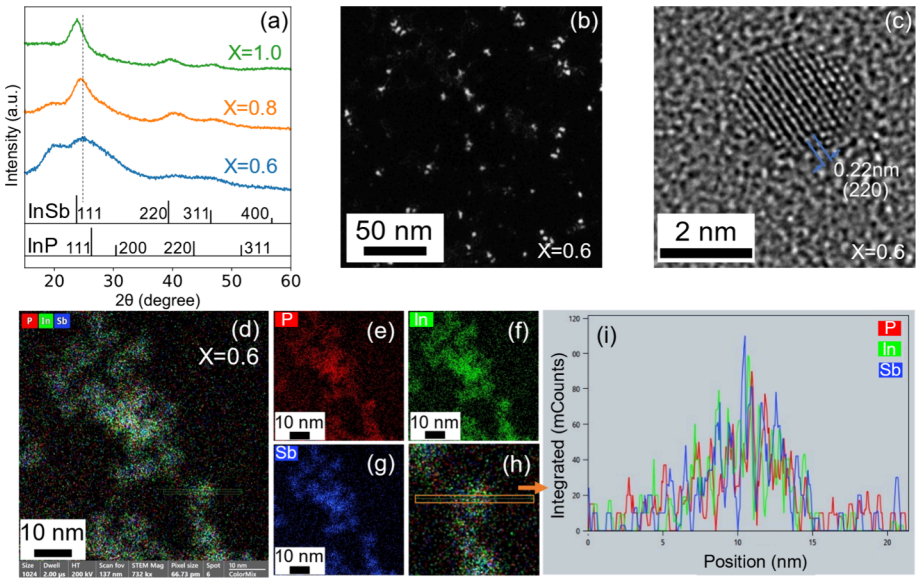

Figure 1. (a) XRD patterns of $InP_{1-x}Sb_x$ QDs synthesized from Sb−TOP system (blue: Sb/In = 0.3 feed ratio, orange: Sb/In = 0.5 feed ratio) and Sb−OlNH system (green). The lattice constants calculated from the diffraction peaks were 0.635 (orange) and 0.623 nm (blue). (b) HAADF-STEM and (c) HR-TEM images of the $InP_{0.4}Sb_{0.6}$ QDs. (d−f) Absorption and PL spectra of $InP_{1-x}Sb_x$ QDs with chemical composition X = 0.6. (d) STEM-EDX overlay image of elemental maps in panels (e), (f), and (g), identifying colocalization of In (green), Sb (blue), and P (red) in typical QDs. (h) Image cropped from the area within the white frame in panel (d). (i) Corresponding line profile of P, In, and Sb EDX signal intensities acquired along the orange line in panel (h).

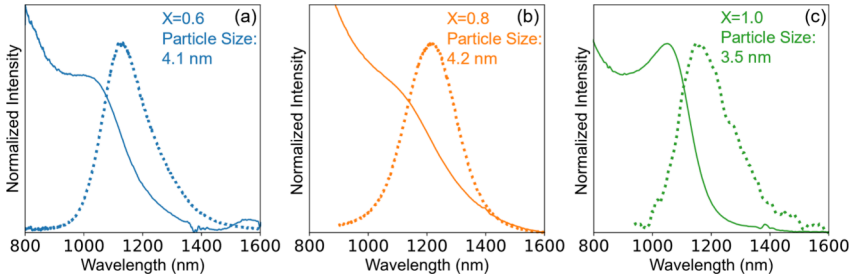

Figure 2. (a−c) Absorption and PL spectra of $InP_{1-x}Sb_x$ QDs with chemical composition X = 0.6−1.0.

significantly affect particle size within experimental error. As highlighted in Figure 1c, high-resolution imaging shows well-defined facets composed of low-index planes such as {111} and {110}, confirming the absence of amorphous domains. The measured lattice spacing (∼0.62 nm) lies between those of bulk InSb (∼0.65 nm) and InP (∼0.59 nm) and agrees well with values extracted from XRD.

STEM-EDX elemental mapping demonstrates homogeneous distributions of In, P, and Sb within individual particles, verifying the formation of genuine anion-alloyed $InP_{1-x}Sb_x$ QDs rather than physical mixtures of InP and InSb (Figure 1d−g). In addition, a EDX line profile acquired across single particles do not exhibit core−shell-like elemental distributions or abrupt compositional transitions (Figure 1h,i).

For comparison, the Sb−OlNH system produced phase-pure InSb QDs (x = 1) with a mean diameter of 4.1 ± 0.9 nm. To further substantiate alloy formation, XPS was conducted on $InP_{1-x}Sb_x$ QDs (x = 0.8−0.6) (see Figure S10, Supporting Information). The In $3d_{5/2}$ binding energies of bulk InSb and InP are 443.5−444.0 eV[16,31] and 444.6−444.7 eV[41,42] respectively. As shown in Panels (b)−(c), the In $3d_{5/2}$ peak shifts progressively from 444.0 to 444.5 eV as the Sb/In feed ratio decreases (x = 0.8 → 0.6), consistent with the higher electronegativity of phosphorus.

The continuous shift of the In $3d_{5/2}$ binding energy with composition indicates a gradual change in the chemical environment surrounding the indium atoms, supporting the formation of an alloy structure. Indeed, Pietra et al. reported a continuous shift of the In 3d peak with increasing Zn content in In_xZn_yP QDs,[43] which they interpreted, in combination with XRD analysis, as evidence of alloy formation. The systematic shift of the In 3d peak observed in this study similarly provides strong support for the formation of an anion-alloyed QD structure.

Figure 2a−c shows the SWIR absorption and PL spectra of $InP_{1-x}Sb_x$ QDs with x = 0.6, 0.8, and 1.0, each exhibiting the characteristic band-edge emission expected for direct bandgap III−V QDs. The asymmetry of the PL spectrum was revealed by time-resolved PL measurements to originate from the size distribution (Figure S11, Supporting Information). When the composition was varied from x = 0.6 to 0.8 while maintaining a comparable particle size of ∼4.2 nm (Figure S9, Supporting Information), the PL peak red-shifted from 1125 to 1220 nm, reflecting increased Sb incorporation within the alloyed lattice. These results demonstrate that the optical response of the QDs can be systematically tuned through precise control of the anion composition. Although QDs with $x \leq 0.6$ were also accessible and emitted near 650 nm, their separation from InP

https://doi.org/10.1021/acs.chemmater.5c03273
Chem. Mater. 2026, 38, 3486−3495

Table 1. Comparison of Reactants for QD Synthesis and Synthetic Yields of the Resultant Mother Sample[a]

	In source	Sb source	reductant	solvent	mother sample	synthetic yield
previous work InSb QDs	$InCl_3$	$SbCl_3$	SH	$OlNH_2$	InSb	13%
this work InSb QDs	$In(Palm)_3$	Sb−$OlNH_2$	$P(NMe_2)_3$	ODE	InSb	40%
this work $InP_{1-x}Sb_x$ QDs	$In(Palm)_3$	Sb−TOP	$P(NMe_2)_3$	ODE	$InP_{1-x}Sb_x$	36%

[a]The synthetic yields were calculated based on the Sb content in the QDs.

Scheme 2. Reaction Scheme for InSb Formation[a]

$$In(RCOO)_3 + SbCl_n{-}L + 3[P(OlNH)_3)] \longrightarrow InSb + 3P(V)$$

[a]$In(RCOO)_3$ and $SbCl_n$−L are reduced by three equivalents of $P(NHOl)_3$ to form InSb and oxidized P(V) species. Here, L represents coordinating ligands (OlNH or TOP) bound to $SbCl_n$.

QDs was challenging, resulting in broadened PL features (Figure S12, Supporting Information). InSb QDs (x = 1.0) with an average diameter of 3.5 nm (Figure S9c, Supporting Information) displayed a PL peak at 1161 nm (1.07 eV), consistent with the established size-bandgap relationship for InSb QDs.[44] The corresponding absorption spectrum exhibited a well-defined excitonic peak with a pronounced valley depth of 0.16.

The size-dependent PL tunability of $InP_{1-x}Sb_x$ QDs is shown in Figure S13. Size control can be achieved by varying the type of saturated fatty acid used during synthesis, and replacing palmitic acid with lauric acid resulted in an approximately 70 nm redshift of the PL emission. In addition, in syntheses employing metal halide-based additives, a tendency toward the formation of relatively larger particles has been reported compared to saturated fatty acid−based systems; accordingly, the addition of $ZnCl_2$ during synthesis enabled a further redshift of the emission wavelength up to 1380 nm (see Figure S13c). Furthermore, as shown in Figure S14, the PL emission wavelength was tuned over a broad spectral window ranging from 860 to 1380 nm by controlling the composition and particle size. Notably, PL peaks emerging in the 800−970 nm region bridge the photon energy gap between the tunable spectral ranges of InP and InSb QDs. A trend toward narrower fwhm values was also observed as the emission wavelength red-shifted. This behavior can be explained by the effective mass approximation (EMA), which describes the size dependence of the bandgap in semiconductor QDs. As particle size increases, the bandgap becomes less sensitive to size variations, leading to a narrower emission energy distribution even with a similar size dispersion.

The absolute PLQYs of the $InP_{1-x}Sb_x$ QDs, measured by standardized integrated method, ranged from 0.1 to 1.3% (Figure S15, Supporting Information), comparable to values reported for unshelled III−V QDs, such as InP,[15] InAs,[45] and InSb.[32] No significant variation in PLQY was observed for compositions of x = 0.6, 0.8, and 1.0. Considering the uniformly low emission efficiencies, nonradiative recombination pathways—most likely associated with surface states—appear to dominate over compositional effects within this range (Table S3, Supporting Information). These results indicate that improving surface passivation is essential to enhance the emission efficiency, and the development of a type-I core−shell structure will therefore be required to achieve bright luminescence.

To the best of our knowledge, no previous study has reported the synthetic yield of colloidal InSb QDs. We therefore benchmarked the yield obtained here against that of our previously reported coreduction method (see Table 1).[4,46] Under the conventional protocol, substantial formation of coarse InSb crystalline precipitates led to modest yield of only 13%. In striking contrast, the yield increased to 40% for the InSb QDs synthesized using the Sb−OlNH system and to 36% for the alloyed $InP_{1-x}Sb_x$ QDs produced using the Sb−TOP system—values that are notably high for III−V QDs. The improved yield is attributed to the suppression of insoluble precipitate formation, and it is considered that saturated fatty acids such as PA, employed as ligands in this study, suppressed particle coarsening. Importantly, both synthetic routes avoid hazardous metal-hydride reductants, providing safer and more scalable pathway toward high-throughput production.

DISCUSSION

To date, all attempts to use $P(NMe_2)_3$ as a reducing agent in ODE have consistently failed in the synthesis of III−V QDs. For example, introducing $P(NMe_2)_3$ into indium acetate-based InP QD syntheses resulted in no QDs formation.[47] This lack of reactivity can reasonably be attributed to the inability of the intermediate $P(OlNH)_3$—generated via transamination between $P(NMe_2)_3$ and primary amines (see eq 3)—[21,38] participate in the reaction network.

$$P(NMe_2)_3 + 3OlnH_2 \rightarrow 3P(OlnH)_3 + 3Me_2NH \quad (3)$$

In the present study, the reaction was conducted in ODE using $In(Palm)_3$ and Sb−L (L = $OlNH_2$ or TOP) as precursors (see Sections S1 and S2, Supporting Information)), while $P(OlNH)_3$ was supplied through the prereaction of $OlNH_2$ with $P(NMe_2)_3$. To confirm the reducing ability of $P(OlNH)_3$, a mixture of $SbCl_3$, TOP, and $P(OlNH)_3$ was heated at 190 °C, and the resulting solution was analyzed by ^{31}P NMR spectroscopy (see Figure S16). The peak observed around 100 ppm is attributed to unreacted transaminated species, whereas the peak at approximately 30 ppm corresponds to $P(NHOl)_4Cl$ formed by oxidation of $P(OlNH)_3$. These results indicate that the overall transformation of the reaction can be explained by the pathway shown in Scheme 2. In this scheme, the oxidation of three equivalents of phosphorus from P(+III) to P(+V) provides the reducing equivalents required to convert both In(+III) and Sb(+III) to their zerovalent states, thereby initiating InSb nucleation. Experimentally, decreasing $OlNH_2$:$P(NMe_2)_3$ molar ratio below 3 reduced the formation of $P(OlNH)_3$, resulting in insufficient reduction of the trivalent cations and, consequently, a markedly lower synthetic yield of InSb QDs. These observations strongly support the reaction pathway proposed in Scheme 2.

https://doi.org/10.1021/acs.chemmater.5c03273
Chem. Mater. 2026, 38, 3486−3495

The Sb−TOP complex was found to be stable at room temperature and served as a soluble antimony precursor. Upon heating above 130 °C, however, the solution gradually darkened, indicating the onset of elemental antimony formation. This reduction proceeded more slowly than that observed for the analogous Sb−DPP complex. To elucidate the coordination environment of the Sb−TOP adduct and its role in nucleation, we began by analyzing it using ^{31}P NMR. Figure S17 shows the ^{31}P NMR spectra of free TOP and of the antimony complex formed by heating a 1:3 mixture of $SbCl_3$ and TOP at 190 °C for 2 min. Free TOP exhibits a resonance at −31 ppm (orange). After heating, the reaction mixture displays four distinct peaks at −16, 11, 39, and 106 ppm, with no detectable signal from unbound TOP, indicating complete coordination of TOP to $SbCl_3$. The resonances at 11, 39, and 106 ppm are consistent with the stepwise oxidation of phosphorus from the +III to the +V oxidation state, in agreement with previous report.[38] The broad feature at −16 ppm is assigned to the Sb−TOP complex, as discussed below. Importantly, these results suggest that TOP coordinated to $SbCl_3$ undergoes gradual oxidation from P(+III) to P(+V), concomitantly donating electrons that are likely accepted by Sb(+III), thereby facilitating its reduction to elemental Sb(0).

In the previous studies, chalcogenide anions such as sulfur, selenium, and tellurium were shown to readily form complexes with TOP, which have been widely employed as anion precursors in the synthesis of compound semiconductor QDs.[48,49] In contrast, to our knowledge, no reports have described the formation of cationic complexes between $SbCl_3$ and TOP, nor has the structural nature of such species been elucidated. Considering possible coordination modes, $SbCl_3$−TOP species may adopt either a neutral $SbCl_3$−TOP_x formulation or a cationic $[SbCl_{3-x}$−$TOP_x]^{x+}$ structure featuring partial chloride dissociation. If the former structure were operative, Sb−Cl bond cleavage at 130 °C would be unlikely; the latter appears more plausible. Under this assumption, chloride dissociation occurs, yet the Sb−TOP interaction remains weak and thermally labile. Collectively, our results indicate that the Sb−TOP complex represents a previously unrecognized class of cationic Sb(+III) precursors.

To elucidate the mechanisms underlying the suppression of InSb formation and the selective generation of alloyed $InP_{1-x}Sb_x$ QDs, we investigated the coordination environment of Sb−TOP. TOP solutions with stepwise additions of $SbCl_3$ were compared with $InCl_3$−TOP system as a reference (see Figure S18, Supporting Information). Unlike $InCl_3$, which is poorly soluble in TOP, $SbCl_3$ dissolves readily, forming homogeneous solutions. ^{31}P NMR spectra (see Figure 3) of these solutions reveal a single resonance across the entire Sb/TOP molar ratio range, in contrast to the multiple species observed for $InCl_3$−TOP. As the Sb/TOP ratio increases, the peak shifts downfield, reflecting stronger Sb(+III)−P interactions and reduced electronic shielding. The single resonance and its compositional dependence indicate rapid exchange between free and coordinated TOP, supporting a model in which chloride dissociation occurs concomitantly with coordination of phosphorus lone pairs to antimony.

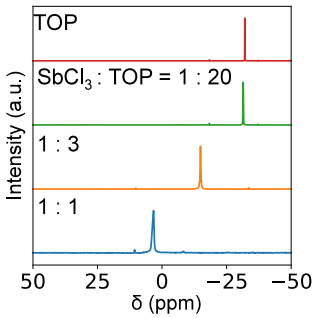

Figure 3. ^{31}P NMR spectra of TOP/$SbCl_3$ mixtures with molar ratios of 20, 3, and 1, respectively.

While the ^{31}P NMR results clearly demonstrate the dynamic coordination of TOP to Sb(+III), they do not provide direct information regarding the behavior of the chloride ligands. To address this, EXAFS measurements were performed to prove the local coordination environment of antimony in the presence of TOP. The analysis reveals substantial changes in antimony coordination upon complex formation. In the XANES region (Figure 4a), the unaltered absorption edge confirms that the oxidation state of antimony remains +III. However, the dampened oscillations and reduced white-line intensity for the $SbCl_3$: TOP samples indicate a perturbation of the original coordination geometry. In Figure 4b, the EXAFS oscillation amplitude of the Sb−TOP complex is markedly lower than that of crystalline $SbCl_3$, suggesting significant alterations in both coordination number and Sb−Cl bond distances. These results indicate the existence of a dynamic equilibrium in which chloride ligands are partially and reversibly substituted by TOP molecules. Under these conditions, chloride anions remain in solution, and the rapid exchange between Sb−Cl and Sb−TOP interactions result in an averaged, structurally disordered local environment. The corresponding *R*-space spectra (Figure 4c) show a pronounced Sb−Cl peak (~2.1 Å) in crystalline $SbCl_3$ that diminishes and broadens with increasing TOP content, while a shoulder at ~2.4 Å (red arrow) grows, consistent with Sb−P coordination. These observations corroborate the NMR-derived inference of dynamic ligand exchange and partial chloride dissociation (Figure 3). Based on EXAFS fitting (Figures S19 and S20, Supporting Information), a plausible coordination model for the $SbCl_3$:TOP = 1:3 system involves one chloride ligand and three TOP molecules arranged around the Sb(+III) center, forming a distorted tetrahedral geometry. The Sb−P coordination number was determined to be 2.9, reflecting the nominal stoichiometry of the precursor mixture, while the residual Sb−Cl coordination number of 0.7 supports the retention of a single chloride ligand. These results are consistent with the formation of a $[SbCl(TOP)_3]^{2+}$-type complex.[50] The steric bulk of the TOP ligands likely limits the coordination number to four. The EXAFS-derived bond lengths of 2.41 ± 0.01 Å for Sb−Cl and 2.59 ± 0.01 Å for Sb−P agree with reported values for these ligand types, supporting the coexistence of both interactions.[51] The slightly elongated Sb−P bond, along with the moderate thermal disorder in the Sb−P shell (σ^2 = 0.0083 Å^2), suggests a flexible, solution-phase complex, consistent with the dynamic coordination behavior inferred from the ^{31}P NMR study. Importantly, the formation of a well-dispersed and labile Sb−TOP complex ensures efficient delivery of reactive Sb(+III) species into the reaction medium. Its thermal instability is a critical factor enabling interaction with the In−P system under the synthesis conditions, thereby providing a favorable pathway for the formation of $InP_{1-x}Sb_x$ alloyed QDs. As discussed above, the Sb−TOP complex promotes the reduction of Sb(+III) to metallic antimony, while $P(NMe_2)_3$ primarily functions to

https://doi.org/10.1021/acs.chemmater.5c03273
Chem. Mater. 2026, 38, 3486−3495

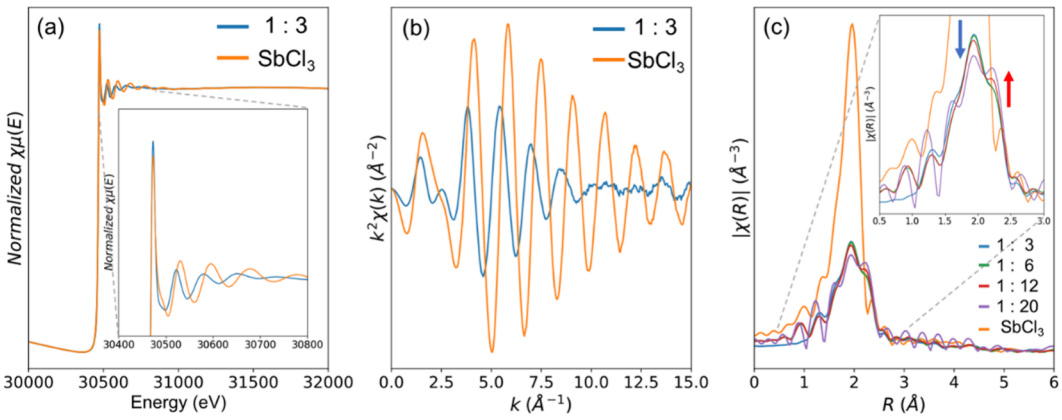

Figure 4. XAFS spectra: (a) XANES and (b) $k^2\chi(k)$ spectra of the $SbCl_3$ and the TOP/$SbCl_3$ mixture with molar ratio of 3. (c) FT-EXAFS spectra of $SbCl_3$ mixed with TOP at various molar ratios (1:3, 1:6, 1:12, and 1:20), showing changes in the local coordination environment around Sb upon complexation with TOP.

Scheme 3. Formation of $InP_{1-x}Sb_x$ Proceeds Through the Following Steps: (a) Sb(0) is Generated Through the Reduction of Sb(+III) by TOP; (b) $P(NMe_2)_3$ Reduces the In Precursor to Produce In(0), Which Subsequently Reacts with Sb(0) to Form InSb Units; Because $P(NMe_2)_3$ Remains in Excess under the Reaction Conditions, InP Units Were Formed Simultaneously; and (c) Formation of $InP_{1-x}Sb_x$ QDs Can Be Attributed to Thermally Induced Interdiffusion between InP and InSb Units

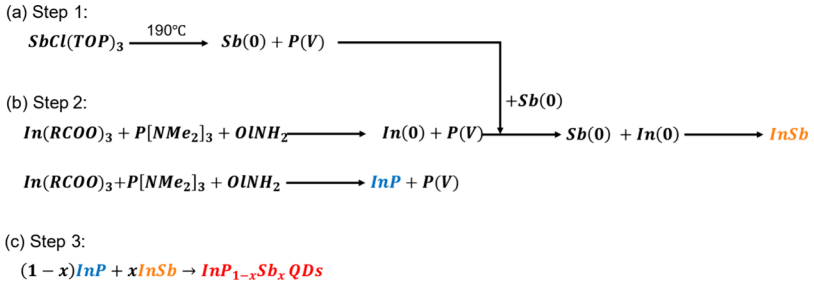

reduce $In(Palm)_3$. Concurrently, the reaction environment facilitates the disproportionation of tris(oleylamino)-phosphine—generated from the interaction between $OlNH_2$ and $P(NMe_2)_3$—thereby increasing the availability of reduced phosphide species. Supporting this interpretation, InP QDs were observed as minor byproducts exclusively when TOP served as the coordinating ligand. To evaluate whether TOP could also reduce the indium precursor, a control reaction was conducted under identical conditions in the absence of $P(NMe_2)_3$. XRD analysis of the resulting products revealed metallic antimony, confirming that TOP alone is incapable of reducing the indium precursor, and thus, cannot independently generate InSb or $InP_{1-x}Sb_x$. These observations underscore the essential role of $P(NMe_2)_3$ in reducing indium precursors.

Based on these findings, a mechanistic pathway is proposed in Scheme 3, in which multiple key reactions proceed concurrently during QD formation. The first step involves the reduction of Sb(+III) in the Sb−TOP complex to metallic Sb (Scheme 3a). In this process, $P(NMe_2)_3$ plays a minimal role due to the steric shielding imposed by the $[SbCl(TOP)_3]$ complex. Consequently, the reduction of Sb(+III) is predominantly mediated by TOP, which undergoes mild oxidation to P(+V), consistent with the ^{31}P NMR observations (Figure S17). The second step (Scheme 3b) represents the reduction of the indium precursor by $P(NMe_2)_3$, yielding metallic indium and promoting the formation of InP units. Formation of metallic indium is directly observed in the insoluble byproducts obtained at a Sb/In feed ratio of 0.2 (Figure S21, Supporting Information). The resulting In(0) subsequently reacts with Sb(0) to generate InSb units, as depicted in Scheme 3a. In parallel, the reaction between $In(Palm)_3$ and $P(NMe_2)_3$ produces InP units, with the process strongly influenced by the relative concentration of $P(NMe_2)_3$. Since TOP reduces Sb(+III), the consumption of $P(NMe_2)_3$ is partially suppressed, ensuring sufficient phosphine availability for InP formation. Additionally, steric hindrance from the tetrahedral $[SbCl(TOP)_3]$ complex further impedes the reduction of antimony by $P(NMe_2)_3$, leaving excess phosphine in solution and promoting InP generation. In contrast, in the Sb−OlNH system, reduction of both antimony and indium precursors proceeds rapidly, resulting in swift $P(NMe_2)_3$ consumption and suppression of InP formation. Finally, as the reaction progresses, interparticle alloying between InSb and InP units occurs, giving rise to $InP_{1-x}Sb_x$ QDs (Scheme 3c). According to this mechanism, extended reaction times should facilitate further alloying, eventually eliminating the InP phase and yielding phase-pure $InP_{1-x}Sb_x$ QDs. To test this prediction, the reaction time was prolonged, and the PL spectra of the resulting products were measured (Figure S22, Supporting Information). As anticipated, the InP emission peak disappeared entirely, replaced by a single broad emission band, confirming the proposed alloying mechanism.

CONCLUSIONS

In this work, we report the colloidal synthesis of $InP_{1-x}Sb_x$ QDs ($0.6 \leq x \leq 1$) using $P(NMe_2)_3$ as both the phosphorus source and a reductant, circumventing the need for hazardous metal-hydride reagents. While $P(NMe_2)_3$ primarily reduces the

https://doi.org/10.1021/acs.chemmater.5c03273
Chem. Mater. 2026, 38, 3486−3495

indium and antimony precursors, its role as a P(−III) source depends critically on the coordination environment of the $SbCl_3$ precursor. In particular, the Sb−TOP complex enables formation of $InP_{1-x}Sb_x$ QDs ($0.6 \leq x < 1$), as its low thermal stability facilitates partial reduction of Sb(+III) to Sb(0), generating a reaction medium conductive to P(−III) species formation. NMR and EXAFS analyses demonstrate that the Sb−TOP complex exists in a dynamic equilibrium between TOP- and Cl-bound states with EXAFS fitting indicating an average coordination of three TOP ligands and 0−1 chloride per Sb center, rationalizing its lability. In contrast, in the Sb−OlNH system, $P(NMe_2)_3$ is primarily consumed in reducing indium and antimony precursors, yielding phase-pure InSb QDs. These results establish a safe and versatile synthetic platform for $InP_{1-x}Sb_x$ QDs and highlight the importance of precursor design in controlling reaction pathways.

The strategy of controlling the coordination environment of pnictogen precursors demonstrated in this study may provide a useful design guideline for other III−V systems, including Ga-based precursors that are difficult to handle. Furthermore, although the PLQY of $InP_{1-x}Sb_x$ QDs reached up to 1.3%, further improvement is expected through core−shell engineering. Selecting shell materials with relatively close lattice constants, such as ZnTe, or tuning the composition of $InP_{1-x}Sb_x$ to improve lattice matching are viable strategies. Enhancing the PLQY would expand the potential of these QDs in photodetectors, LED devices, and other SWIR applications.

EXPERIMENTAL SECTION

Reagents and Materials

Indium(III) acetate [$In(Ac)_3$, 99.99%, Aldrich], zinc acetate [$Zn(Ac)_2$, 99.99%, Aldrich], antimony(III) chloride [$SbCl_3$, 99.95%, Aldrich], zinc oxide [ZnO, 99.999%, Aldrich], tris(dimethylamido)-antimony(III) [$Sb[NMe_2]_3$, 99.99%, Aldrich], palmitic acid [PA, 98%, Tokyo Chemical Industry], tris(dimethylamino)phosphine [$P[NMe_2]_3$, 97%, Aldrich], 1-octadecene [ODE, 90%, Aldrich], trioctylphosphine [TOP, 97%, Aldrich], oleylamine [$OlNH_2$, 80−90%, Thermo Scientific Chemicals], tris(trimethylsilyl)-phosphine [$(TMS)_3P$, 98% Strem Chemicals] and oleic acid [OA, 90%, Aldrich] were used without further purification. The purity of argon gas used for the synthesis was 99.999%.

Preparation of Sb-TOP Precursor

$SbCl_3$ (0.045−0.075 mmol) was dissolved in TOP (1 mL) by stirring the mixture at 50 °C for 10 min in an Ar-filled glovebox that was continuously monitored to maintain both oxygen and water levels of $O_2 \leq 1$ ppm and $H_2O \leq 5$ ppm.

Preparation of Sb-OlNH Precursor

$SbCl_3$ (0.045−0.075 mmol) was dissolved in $OlNH_2$ (1 mL) by stirring the mixture at 70 °C for 12 h in an Ar-filled glovebox that was continuously monitored to maintain both oxygen and water levels of $O_2 \leq 1$ ppm and $H_2O \leq 5$ ppm.

Preparation of $P(NMe_2)_3$-OlNH

$P(NMe_2)_3$ (1.8∼3.0 mmol) was dissolved in 1 mL of OLA at room temperature in a same glovebox.

Preparation of $P(TMS)_3$-TOP

According to our protocol reported before,[26] $P(TMS)_3$ (0.12 mmol) was dissolved in 1 mL of TOP at room temperature in a glovebox to prepare a $P(TMS)_3$-TOP solution. This stock solution was stored overnight in an Ar-filled vial before use.

Preparation of ZnOA-ODE

ZnO (2.0 mmol) and OA (8.0 mmol) were mixed with 10 mL of ODE in a 50 mL three-necked flask. The mixture was degassed at 120 °C for 2 h under vacuum conditions, filled with Ar gas, and then the mixture was quickly heated to 290 °C and held for 1 h, after which the mixed solution became a transparent, signifying the formation of Zn-oleate (ZnOA). After that, the solution was cooled down to room temperature and stored in Ar-filled vial until the use.

Synthesis of $InP_{1-x}Sb_x$ QDs

0.15 mmol of $In(Ac)_3$, 0.075 mmol of $Zn(Ac)_2$ and PA (0.575 mmol) were mixed with 6.3 mL of ODE in a 50 mL three-necked flask, with the reflux condenser attached to the central neck and connected to the Schlenk line. Using an oil rotary vacuum pump, the flask was degassed and purged with Ar gas five times under vacuum conditions below 60 Pa. Degassing of the mixture was performed under vacuum conditions at 120 °C for 12 h. After filled with Ar gas, the solution was heated to 190 °C in 4 min. The preprepared Sb−TOP or Sb−OlNH precursor solution was rapidly injected in its entirety into the flask under flowing Ar. In the case of the Sb−TOP precursor, the initially colorless solution turned light brown upon injection, whereas the solution remained transparent when the Sb−OlNH precursor was used. After 2 min, the preprepared $P[NMe_2]_3/OlNH_2$ mixture was rapidly injected into the flask in its entirety, resulting in a color change of the solution from light brown to black. The flask was further heated to 280 °C within 5 min and maintained at 280 °C for 2 min. The heating mantle heater was removed, and the flask was allowed to cool under air flow to approximately 200 °C. The flask was then further cooled with water until the temperature fell below 100 °C. The total cooling time from 280 °C to below 100 °C was approximately 2 min.

Synthesis of InP/ZnS QDs Emitting at 490 nm

The precursor and degassing process were the same as those used for $InP_{1-x}Sb_x$ QDs. The degassed mixture was cooled to room temperature and purged with Ar gas. The $P(TMS)_3$-TOP solution was injected into the flask, and the resulting mixture was degassed under vacuum at 40 °C for 10 min. After refilling with Ar gas, the solution was heated at 300 °C for 5 min. For shell growth, the InP solution was cooled to 230 °C, followed by the injection of 2 mL of ZnOA and 250 μL of DDT, and maintained at this temperature for 20 min. To further increase the shell thickness, the previous procedure was repeated twice at an elevated temperature of 240 °C. After achieving the desired shell thickness, the solution was cooled to room temperature.

Synthesis of InP/ZnS QDs Emitting at 600 nm

Synthesis of InP/ZnS QDs emitting at 600 nm: In a 50 mL three-neck round-bottom flask, 0.5 mmol of $InCl_3$, 0.5 mmol of $ZnCl_2$, and 7.2 mL of oleylamine were added. The flask was evacuated under vacuum at 50 °C for 25 min. Subsequently, the solution was rapidly heated to 220 °C under an Ar atmosphere, followed by the swift injection of 5 mmol of $P(NMe_2)_3$. After 30 min, the temperature was raised to 230 °C, and the shell was grown using the same method as for the InP/ZnS QDs emitting at 500 nm. Once shell formation was complete, the solution was cooled to room temperature.

Synthesis of InP/ZnS QDs Emitting at 760 nm

Followed by the hot-injection method reported by Ranjana et al.,[52] we prepared the InP/ZnS QDs emitting to In a 50 mL three-neck round-bottom flask, 0.5 mmol of In(I) Cl, 0.7 mmol of TOP, and 7.2 mL of oleylamine were added. The flask was evacuated under vacuum at 50 °C for 25 min. Subsequently, the solution was rapidly heated to 220 °C under an Ar atmosphere, followed by the swift injection of 0.5 mmol of $P(NMe_2)_3$ dissolved in 0.5 mL of ODE. After 30 min, the temperature was raised to 230 °C, and the shell was grown using the same method as for the InP/ZnS QDs emitting at 500 nm. Once shell formation was complete, the solution was cooled to room temperature.

Purification of QDs

The as-synthesized solution (named "product" in the Figure S1) was transferred to a centrifuge tube and centrifuged at 9000 rpm for 10 min. The precipitate and supernatant liquid were separated into respective centrifuge tubes. Acetone 20 mL was added to the entire supernatant solution, and the mixture was centrifuged at 9000 rpm for 5 min. The supernatant was then discarded. The precipitate was

https://doi.org/10.1021/acs.chemmater.5c03273
Chem. Mater. 2026, 38, 3486−3495

redispersed in 5 mL of hexane and 15 mL of methanol was added until the solution became turbid, followed by centrifugation at 9000 rpm for 5 min. This washing process was repeated two times to prepare a mother sample as defined in Figure S1.

Separation of $InP_{1-x}Sb_x$ QDs

Separation of $InP_{1-x}Sb_x$ QDs was performed by modifying the centrifugation process reported in elsewhere.[53] The mother sample was subjected to the centrifugation process for separation of $InP_{1-x}Sb_x$ QDs from other kinds of QDs. The mother sample was dispersed in a 5 mL of hexane. The mother solution was centrifugated at 9000 rpm with incremental addition of ethanol by 0.5 m as shown in Figure S1. For example, the fraction obtained with hexane 5 mL and ethanol 2.5∼3.5 mL was designated as "Sample A" in Figure S1. The centrifugations were all performed at 9000 rpm for 5 min.

Despite this separation process, in rare cases weak emission attributable to InP QDs was still observed in Sample A after PL measurements. In such cases, the contribution could be effectively removed by repeating the centrifugation under the same conditions (hexane 5 mL and ethanol 3.5 mL for Sample A).

Characterization

X-ray powder diffraction (XRD) patterns were measured on MiniFlex 600 (Rigaku, Japan). High-resolution transmission electron microscopic (HR-TEM) images were obtained from JEOL-JEM 2100 microscope, operating at 200 kV, equipped with energy dispersive X-ray (EDX) elemental analysis system. Additional high-resolution STEM imaging and elemental mapping were conducted using a Spectra Ultra S/TEM (Thermo Fisher Scientific) instrument operated at 200 kV to achieve improved spatial resolution in compositional analysis. Some of the samples were studied by X-ray photoelectron spectroscopy (XPS; Ulvac, PHI Quantera) using AlKα (E = 1486.6 eV) radiation. The binding energy (BE) scale was calibrated to provide Au $4f_{7/2}$ = 83.9 eV and Cu $2p_{3/2}$ = 932.8 eV. The X-ray source was operated at 10 mA and 12 kV. The core-level signals were obtained at a photoelectron takeoff angle of 90° (with respect to the sample surface). The BE scales were referenced to 284.6 eV as determined by the locations of the maximum peaks on the C 1s spectra of hydrocarbon, associated with an adventitious contamination. Optical absorption and emission properties were measured with colloidal solution of the QDs. Optical absorption spectra were measured by a UV−vis spectrophotometer (JASCO V-650, Japan) with an integrated sphere. Photoluminescence (PL) measurement was carried out using a modular double grating Czerny−Turner monochromator and an iHR 320 emission monochromator (1200 lines/mm of gratings) coupled to a photomultiplier tube (PMT) on a NanoLog Horiba Jovin Yvon spectrofluorometer with a 450 W xenon arc lamp. The spectral resolution of the system is around 0.3 nm. To avoid scattered excitation lights, a cut filter for 395 nm-light was placed in front of the monochromator-PMT setup. The absolute PL quantum yields (QYs) were measured at room temperature using the QY measurement extended system C13534−01 from Hamamatsu Photonics Co., Ltd. with a 150 W xenon lamp coupled to a monochromator for wavelength discrimination, an integrating sphere as a sample chamber, and a multichannel analyzer for signal detection. Nuclear magnetic resonance (NMR) spectroscopy was employed to investigate the coordination environment of phosphorus in $SbCl_3$−TOP mixtures. All spectra were recorded on a 600 MHz NMR spectrometer (JNM-ECZL600R, JEOL) using toluene-d_8 as the solvent. The $SbCl_3$ and TOP solutions were prepared in an argon-filled glovebox to prevent hydrolysis and oxidation, and were sealed in airtight NMR tubes prior to measurement. The molar ratio of TOP to Sb was systematically varied between 3 and 20. The ^{31}P NMR spectra were collected at room temperature without further purification or addition of reference standards. EXAFS measurements were conducted at the AR-NW10A beamline of the Photon Factory Advanced Ring (PF-AR, 6.5 GeV, 50 mA) at the High Energy Accelerator Research Organization (KEK), Tsukuba, Japan. A Si (311) double-crystal monochromator was used to monochromatize the incident X-ray beam. The samples were prepared by mixing $SbCl_3$ with TOP, adjusting the TOP/Sb molar ratio in the range of 3 to 20. The mixtures were measured in liquid phase, and antimony K-edge EXAFS spectra were recorded in transmission mode. The energy scale was calibrated using a standard pellet of Sb_2O_3 mixed with boron nitride, by defining the first inflection point of the antimony K-edge as 30,492.0 eV. The XAFS spectra were processed using the ATHENA software in the Demeter package.[54] The spectra were first subjected to background subtraction and normalization, followed by Fourier transform of the k^3-weighted $\chi(k)$ functions to obtain the radial structure function in R-space. EXAFS oscillations were fitted using the following equation implemented in the Artemis software:

$$\chi(k) = S_0^2 \sum_j \frac{N_j F_j(k) \exp(-2k^2\sigma_j^2)}{kR_j^2} \sin(2kR_j + \Phi_j(k)) \quad \text{(S1)}$$

In this equation, N_j is the coordination number, R_j is the bond length, S_0^2 is the amplitude reduction factor, and σ_j^2 is the Debye−Waller factor. The terms $F_j(k)$ and $\Phi_j(k)$ represent the backscattering amplitude and phase shift, respectively, both of which were theoretically calculated using the FEFF code based on the structural model of $SbCl_3$.

■ ASSOCIATED CONTENT

Supporting Information

The Supporting Information is available free of charge at https://pubs.acs.org/doi/10.1021/acs.chemmater.5c03273.

Detailed information on synthetic conditions and optical properties of indium pnictides QDs; microscopic observation and elemental mapping results of the precipitate and $InP_{1-x}Sb_x$ QDs; size distributions and PLQY spectra of the $InP_{1-x}Sb_x$ QDs; photographs of $SbCl_3$ mixed with various solvents and XRD profiles of the samples prepared by reaction of these antimony species with indium palmitate; and ^{31}P NMR spectra of pure TOP and TOP mixed with $InCl_3$ (PDF)

■ AUTHOR INFORMATION

Corresponding Authors

Kazuhiro Nemoto − *Research Center for Materials Nanoarchitectonics (MANA), National Institute for Materials Science (NIMS), Tsukuba 305-0047, Japan*; Email: nemoto.kazuhiro@nims.go.jp

Naoto Shirahata − *Research Center for Materials Nanoarchitectonics (MANA), National Institute for Materials Science (NIMS), Tsukuba 305-0047, Japan; Graduate School of Chemical Sciences and Engineering, Hokkaido University, Sapporo 060-0814, Japan*; orcid.org/0000-0002-1217-7589; Email: shirahata.naoto@nims.go.jp

Authors

Cong Zhang − *Research Center for Materials Nanoarchitectonics (MANA), National Institute for Materials Science (NIMS), Tsukuba 305-0047, Japan; Graduate School of Chemical Sciences and Engineering, Hokkaido University, Sapporo 060-0814, Japan*

Daiki Kido − *Institute of Materials Structure Science (IMSS), High Energy Accelerator Research Organization (KEK), Tsukuba 305-0801, Japan; Materials Structure Science Program, Graduate Institute for Advanced Studies, SOKENDAI, Tsukuba, Ibaraki 305-0801, Japan*

Daniel Limouchi − *Research Center for Materials Nanoarchitectonics (MANA), National Institute for Materials Science (NIMS), Tsukuba 305-0047, Japan; Graduate School of Chemical Sciences and Engineering,*

https://doi.org/10.1021/acs.chemmater.5c03273
Chem. Mater. 2026, 38, 3486−3495

Hokkaido University, Sapporo 060-0814, Japan; orcid.org/0009-0005-0205-447X

Masaki Takeguchi − *Research Center for Energy and Environmental Materials, NIMS, Tsukuba 305-0047, Japan;* orcid.org/0000-0002-0282-6020

Hong-Tao Sun − *Research Center for Materials Nanoarchitectonics (MANA), National Institute for Materials Science (NIMS), Tsukuba 305-0047, Japan;* orcid.org/0000-0002-0003-7941

Complete contact information is available at: https://pubs.acs.org/10.1021/acs.chemmater.5c03273

Author Contributions

K.N. and C.Z. contributed equally to this work; K.N., C.Z., and N.S. designed research; K.N., C.Z., and H.-T.S. performed research; K.N., C.Z. H.-T.S., and N.S. discussed the result; and K.N. and N.S. wrote the paper. All authors commented on the paper.

Funding

JSPS KAKENHI (grant no. 24K01462, 24K21720, and 24K01278) and Hosokawa Powder Technology Foundation (grant number HPTF24111).

Notes

The authors declare no competing financial interest.

■ ACKNOWLEDGMENTS

A part of this work was supported by "Advanced Research Infrastructure for Materials and Nanotechnology in Japan (ARIM)" of the Ministry of Education, Culture, Sports, Science and Technology (MEXT): Proposal Number JPMXP1224NM5178. The authors thank to the financial support by WPI program, JSPS KAKENHI (grant no. 24K01462, 24K21720, 24K01278, and 25K22207) and Hosokawa Powder Technology Foundation (grant number HPTF24111).

■ ABBREVIATIONS

HR-TEM, high-resolution transmission electron microscopy; HAASF-STEM, high-angle annular dark field scanning transmission electron microscopy; EDX, energy dispersive X-ray spectroscopy; XRD, X-ray powder diffraction; NMR, nuclear magnetic resonance; PL, photoluminescence; fwhm, full width at half-maximum; XPS, X-ray photoelectron spectroscopy

■ REFERENCES

(1) del Alamo, J. A. Nanometre-Scale Electronics with III−V Compound Semiconductors. *Nature* **2011**, *479* (7373), 317−323.

(2) Carey, G. H.; Abdelhady, A. L.; Ning, Z.; Thon, S. M.; Bakr, O. M.; Sargent, E. H. Colloidal Quantum Dot Solar Cells. *Chem. Rev.* **2015**, *115* (23), 12732−12763.

(3) Kim, T.; Lim, S.; Yun, S.; Jeong, S.; Park, T.; Choi, J. Design Strategy of Quantum Dot Thin-Film Solar Cells. *Small* **2020**, *16* (45), No. 2002460.

(4) Chatterjee, S.; Nemoto, K.; Ghosh, B.; Sun, H.-T.; Shirahata, N. Solution-Processed InSb Quantum Dot Photodiodes for Short-Wave Infrared Sensing. *ACS Appl. Nano Mater.* **2023**, *6* (17), 15540−15550.

(5) Nemoto, K.; Watanabe, J.; Yamada, H.; Sun, H.-T.; Shirahata, N. Impact of Coherent Core/Shell Architecture on Fast Response in InP-Based Quantum Dot Photodiodes. *Nanoscale Adv.* **2023**, *5* (3), 907−915.

(6) Liu, Z.; Sun, C.; Wang, Q.; Lu, W.; Liu, Z.; Li, P.; Chen, Y.; Hu, X.; You, H.; Zhang, J.; Hou, X.; Zeng, B.; Li, Q.; Zhu, J.; Dai, N.; Li, Y. Colloidal InSb Quantum Dots Mid-Wave Infrared Photoconductive Detectors via One-Step Strong Acid Surface Treatment Strategy. *Nano Lett.* **2025**, *25* (36), 13549−13556.

(7) Chen, M.; Li, Q.; Bian, Y.; Wang, S.; Hu, B.; Tang, A.; Chen, F.; Lv, Y.; Shen, H. High-Efficiency and Stable Green InP-QLED Enabled by Lowering Electron Injection Barrier. *Adv. Opt. Mater.* **2025**, *13* (6), No. 2402555.

(8) Won, Y.-H.; Cho, O.; Kim, T.; Chung, D.-Y.; Kim, T.; Chung, H.; Jang, H.; Lee, J.; Kim, D.; Jang, E. Highly Efficient and Stable InP/ZnSe/ZnS Quantum Dot Light-Emitting Diodes. *Nature* **2019**, *575* (7784), 634−638.

(9) Pan, Y.-Y.; Pan, J.-L.; Wang, Y.-K.; Liao, L.-S. III-V Quantum Dots: A Multidimensional Exploration from Eco-Friendly Materials to near Infrared Optoelectronic Applications. *Mater. Today* **2025**, *85*, 171−188.

(10) Zhang, W.; Duan, X.; Tan, Y.; Hao, J.; Zhu, H.; Wang, Q.; Yang, H.; Liu, H.; Wang, K.; Wang, Z.; Wang, Y.; Song, Y.; Sun, X. W. Giant Pyramidal Near-Infrared InP/ZnS Quantum Dots with Size Over 15 Nm for Cell Imaging. *Laser Photonics Rev.* **2024**, *18* (10), No. 2400367.

(11) Franke, D.; Harris, D. K.; Chen, O.; Bruns, O. T.; Carr, J. A.; Wilson, M. W. B.; Bawendi, M. G. Continuous Injection Synthesis of Indium Arsenide Quantum Dots Emissive in the Short-Wavelength Infrared. *Nat. Commun.* **2016**, *7* (1), No. 12749.

(12) Wells, R. L.; McPhail, A. T.; Shafieezad, S.; Hallock, R. B. The Use of Tris(Trimethylsilyl)Arsine To Prepare Gallium Arsenide and Indium Arsenide. *Chem. Mater.* **1989**, *1*, 4−6.

(13) Franke, D.; Harris, D. K.; Xie, L.; Jensen, K. F.; Bawendi, M. G. The Unexpected Influence of Precursor Conversion Rate in the Synthesis of III−V Quantum Dots. *Angew. Chem. Int. Ed* **2015**, *54* (48), 14299−14303.

(14) Micic, O. I.; Curtis, C. J.; Jones, K. M.; Sprague, J. R.; Nozik, A. J. Synthesis and Characterization of InP Quantum Dots. *J. Phys. Chem.* **1994**, *98* (19), 4966−4969.

(15) Nemoto, K.; Watanabe, J.; Sun, H.-T.; Shirahata, N. Coherent InP/ZnS Core@shell Quantum Dots with Narrow-Band Green Emissions. *Nanoscale* **2022**, *14* (27), 9900−9909.

(16) Seo, H.; Eun, H. J.; Lee, A. Y.; Lee, H. K.; Kim, J. H.; Kim, S. Colloidal InSb Quantum Dots for 1500 Nm SWIR Photodetector with Antioxidation of Surface. *Adv. Sci.* **2023**, *11*, No. 2306439.

(17) Evans, C. M.; Castro, S. L.; Worman, J. J.; Raffaelle, R. P. Synthesis and Use of Tris(Trimethylsilyl)Antimony for the Preparation of InSb Quantum Dots. *Chem. Mater.* **2008**, *20* (18), 5727−5730.

(18) Harris, D. K.; Bawendi, M. G. Improved Precursor Chemistry for the Synthesis of III−V Quantum Dots. *J. Am. Chem. Soc.* **2012**, *134* (50), 20211−20213.

(19) An, S.; Cho, H.; Jeon, H. B.; Kim, S.-W. InPZnS Alloy Quantum Dots with Tris(Hexylthio)Phosphine as a Dual Anionic Precursor. *Nanoscale* **2018**, *10* (6), 3014−3019.

(20) Stelmakh, A.; Marnieros, G.; Schrader, E.; Nedelcu, G.; Hordiichuk, O.; Rusanov, E.; Cherniukh, I.; Zindel, D.; Grützmacher, H.; Kovalenko, M. V. Acylphosphine Route to Colloidal InP Quantum Dots. *J. Am. Chem. Soc.* **2025**, *147* (13), 11446−11455.

(21) Tessier, M. D.; Dupont, D.; De Nolf, K.; De Roo, J.; Hens, Z. Economic and Size-Tunable Synthesis of InP/ZnE (E = S, Se) Colloidal Quantum Dots. *Chem. Mater.* **2015**, *27* (13), 4893−4898.

(22) Buffard, A.; Dreyfuss, S.; Nadal, B.; Heuclin, H.; Xu, X.; Patriarche, G.; Mézailles, N.; Dubertret, B. Mechanistic Insight and Optimization of InP Nanocrystals Synthesized with Aminophosphines. *Chem. Mater.* **2016**, *28* (16), 5925−5934.

(23) Leemans, J.; Respekta, D.; Bai, J.; Braeuer, S.; Vanhaecke, F.; Hens, Z. Formation of Colloidal In(As,P) Quantum Dots Active in the Short-Wave Infrared, Promoting Growth through Temperature Ramps. *ACS Nano* **2023**, *17* (20), 20002−20012.

(24) Liu, P.; Lou, Y.; Ding, S.; Zhang, W.; Wu, Z.; Yang, H.; Xu, B.; Wang, K.; Sun, X. W. Green InP/ZnSeS/ZnS Core Multi-Shelled Quantum Dots Synthesized with Aminophosphine for Effective Display Applications. *Adv. Funct. Mater.* **2021**, *31* (11), No. 2008453.

(25) Duan, X.; Ma, J.; Zhang, W.; Liu, P.; Liu, H.; Hao, J.; Wang, K.; Samuelson, L.; Sun, X. W. Study of the Interfacial Oxidation of InP Quantum Dots Synthesized from Tris(Dimethylamino)Phosphine. *ACS Appl. Mater. Interfaces* **2023**, *15* (1), 1619−1628.
(26) Long, R.; Chen, X.; Zhang, X.; Chen, F.; Wu, Z.; Shen, H.; Du, Z. Carboxylic-Free Synthesis of InP Quantum Dots for Highly Efficient and Bright Electroluminescent Device. *Adv. Opt. Mater.* **2023**, *11* (6), No. 2202594.
(27) Grigel, V.; Dupont, D.; De Nolf, K.; Hens, Z.; Tessier, M. D. InAs Colloidal Quantum Dots Synthesis via Aminopnictogen Precursor Chemistry. *J. Am. Chem. Soc.* **2016**, *138* (41), 13485−13488.
(28) Maurice, A.; Haro, M. L.; Hyot, B.; Reiss, P. Synthesis of Colloidal Indium Antimonide Nanocrystals Using Stibine. *Part & Part Syst. Charact* **2013**, *30* (10), 828−831.
(29) Kwon, Y.; Yeromina, O.; Cavallo, M.; Silly, M. G.; Pierucci, D.; Lhuillier, E.; Aldakov, D.; Hyot, B.; Reiss, P. Synthesis of NIR/SWIR Absorbing InSb Nanocrystals Using Indium(I) Halide and Aminostibine Precursors. *Adv. Funct. Mater.* **2024**, *34* (40), No. 2403912.
(30) Busatto, S.; de Ruiter, M.; Jastrzebski, J. T. B. H.; Albrecht, W.; Pinchetti, V.; Brovelli, S.; Bals, S.; Moret, M.-E.; de Mello Donega, C. Luminescent Colloidal InSb Quantum Dots from *In Situ* Generated Single-Source Precursor. *ACS Nano* **2020**, *14* (10), 13146−13160.
(31) Zhao, T.; Oh, N.; Jishkariani, D.; Zhang, M.; Wang, H.; Li, N.; Lee, J. D.; Zeng, C.; Muduli, M.; Choi, H.-J.; Su, D.; Murray, C. B.; Kagan, C. R. General Synthetic Route to High-Quality Colloidal III−V Semiconductor Quantum Dots Based on Pnictogen Chlorides. *J. Am. Chem. Soc.* **2019**, *141* (38), 15145−15152.
(32) Liu, W.; Chang, A. Y.; Schaller, R. D.; Talapin, D. V. Colloidal InSb Nanocrystals. *J. Am. Chem. Soc.* **2012**, *134* (50), 20258−20261.
(33) Heiden, Z. M.; Lathem, A. P. Establishing the Hydride Donor Abilities of Main Group Hydrides. *Organometallics* **2015**, *34* (10), 1818−1827.
(34) Srivastava, V.; Dunietz, E.; Kamysbayev, V.; Anderson, J. S.; Talapin, D. V. Monodisperse InAs Quantum Dots from Aminoarsine Precursors: Understanding the Role of Reducing Agent. *Chem. Mater.* **2018**, *30* (11), 3623−3627.
(35) Crisp, R. W.; Grimaldi, G.; De Trizio, L.; Evers, W. H.; Kirkwood, N.; Kinge, S.; Manna, L.; Siebbeles, L. D. A.; Houtepen, A. J. Selective Antimony Reduction Initiating the Nucleation and Growth of InSb Quantum Dots. *Nanoscale* **2018**, *10* (23), 11110−11116.
(36) Imran, M.; Kim, D. B.; Xia, P.; Villanueva, F. Y.; Rehl, B.; Pina, J. M.; Liu, Y.; Zhang, Y.; Voznyy, O.; Kumacheva, E.; Hoogland, S.; Sargent, E. H. Control Over Metal-Halide Reactivity Enables Uniform Growth of InSb Colloidal Quantum Dots for Enhanced SWIR Light Detection. *Adv. Mater.* **2025**, *37* (12), No. 2420273.
(37) Muhammad; Choi, D.; Parmar, D. H.; Rehl, B.; Zhang, Y.; Atan, O.; Kim, G.; Xia, P.; Pina, J. M.; Li, M.; Liu, Y.; Voznyy, O.; Hoogland, S.; Sargent, E. H. Halide-Driven Synthetic Control of InSb Colloidal Quantum Dots Enables Short-Wave Infrared Photodetectors. *Adv. Mater.* **2023**, *35* (46), No. 2306147.
(38) Tessier, M. D.; De Nolf, K.; Dupont, D.; Sinnaeve, D.; De Roo, J.; Hens, Z. Aminophosphines: A Double Role in the Synthesis of Colloidal Indium Phosphide Quantum Dots. *J. Am. Chem. Soc.* **2016**, *138* (18), 5923−5929.
(39) Benyettou, S.; Saib, S.; Bouarissa, N. Materials Properties, Lattice Dynamics and Polaron Characteristics in InSbxP1-x Ternary Alloys. *Mater. Sci. Semicond. Process.* **2021**, *125*, No. 105640.
(40) Degheidy, A. R.; Elkenany, E. B.; Alfrnwani, O. A. Influence of Composition, Temperature and Pressure on the Optoelectronic and Mechanical Properties of InPxSb1-x Alloys. *Comput. Condens. Matter* **2018**, *16*, No. e00300.
(41) Virieux, H.; Le Troedec, M.; Cros-Gagneux, A.; Ojo, W.-S.; Delpech, F.; Nayral, C.; Martinez, H.; Chaudret, B. InP/ZnS Nanocrystals: Coupling NMR and XPS for Fine Surface and Interface Description. *J. Am. Chem. Soc.* **2012**, *134* (48), 19701−19708.
(42) Huang, K.; Demadrille, R.; Silly, M. G.; Sirotti, F.; Reiss, P.; Renault, O. Internal Structure of InP/ZnS Nanocrystals Unraveled by High-Resolution Soft X-Ray Photoelectron Spectroscopy. *ACS Nano* **2010**, *4* (8), 4799−4805.
(43) Pietra, F.; De Trizio, L.; Hoekstra, A. W.; Renaud, N.; Prato, M.; Grozema, F. C.; Baesjou, P. J.; Koole, R.; Manna, L.; Houtepen, A. J. Tuning the Lattice Parameter of In $_x$ Zn $_y$ P for Highly Luminescent Lattice-Matched Core/Shell Quantum Dots. *ACS Nano* **2016**, *10* (4), 4754−4762.
(44) Xie, H.; Zhang, C.; Yang, R.; Xu, J.; Pan, Y.; Yin, X. From Synthesis to Application in Infrared Photodetectors: A Review of InSb Colloidal Quantum Dots. *Laser Photonics Rev.* **2025**, *19* (4), No. 2401204.
(45) Ginterseder, M.; Franke, D.; Perkinson, C. F.; Wang, L.; Hansen, E. C.; Bawendi, M. G. Scalable Synthesis of InAs Quantum Dots Mediated through Indium Redox Chemistry. *J. Am. Chem. Soc.* **2020**, *142* (9), 4088−4092.
(46) Chatterjee, S.; Nemoto, K.; Sun, H.-T.; Shirahata, N. Rational Ligand Design for Enhanced Carrier Mobility in Self-Powered SWIR Photodiodes Based on Colloidal InSb Quantum Dots. *Nanoscale Horiz.* **2024**, *9* (5), 817−827.
(47) Song, W.-S.; Lee, H.-S.; Lee, J. C.; Jang, D. S.; Choi, Y.; Choi, M.; Yang, H. Amine-Derived Synthetic Approach to Color-Tunable InP/ZnS Quantum Dots with High Fluorescent Qualities. *J. Nanopart. Res.* **2013**, *15* (6), 1750.
(48) He, X.-H.; Yin, Y.-L.; Tang, G.; Liu, Y.; Jiang, F.-L. Role of Trioctylphosphine in the Synthesis of Quantum Dots: A Modulator of Nucleation, Growth, and Solubility. *J. Phys. Chem. C* **2023**, *127* (10), 5021−5028.
(49) Shuklov, I. A.; Mikhel, I. S.; Nevidimov, A. V.; Birin, K. P.; Dubrovina, N. V.; Lizunova, A. A.; Razumov, V. F. Mechanistic Insights into the Synthesis of Telluride Colloidal Quantum Dots with Trioctylphosphine-Tellurium. *ChemistrySelect* **2020**, *5* (38), 11896−11900.
(50) Chitnis, S. S.; Peters, B.; Conrad, E.; Burford, N.; McDonald, R.; Ferguson, M. J. Structural Diversity for Phosphine Complexes of Stibenium and Stibinidenium Cations. *Chem. Commun.* **2011**, *47* (45), 12331.
(51) Chitnis, S. S.; Burford, N.; McDonald, R.; Ferguson, M. J. Prototypical Phosphine Complexes of Antimony(III). *Inorg. Chem.* **2014**, *53* (10), 5359−5372.
(52) Yadav, R.; Kwon, Y.; Rivaux, C.; Saint-Pierre, C.; Ling, W. L.; Reiss, P. Narrow Near-Infrared Emission from InP QDs Synthesized with Indium(I) Halides and Aminophosphine. *J. Am. Chem. Soc.* **2023**, *145* (10), 5970−5981.
(53) Taylor, D. A.; Teku, J. A.; Cho, S.; Chae, W.-S.; Jeong, S.-J.; Lee, J.-S. Importance of Surface Functionalization and Purification for Narrow FWHM and Bright Green-Emitting InP Core−Multishell Quantum Dots via a Two-Step Growth Process. *Chem. Mater.* **2021**, *33* (12), 4399−4407.
(54) Ravel, B.; Newville, M. *ATHENA*, *ARTEMIS*, *HEPHAESTUS*: Data Analysis for X-Ray Absorption Spectroscopy Using *IFEFFIT*. *J. Synchrotron Rad* **2005**, *12* (4), 537−541.

https://doi.org/10.1021/acs.chemmater.5c03273
Chem. Mater. 2026, 38, 3486−3495